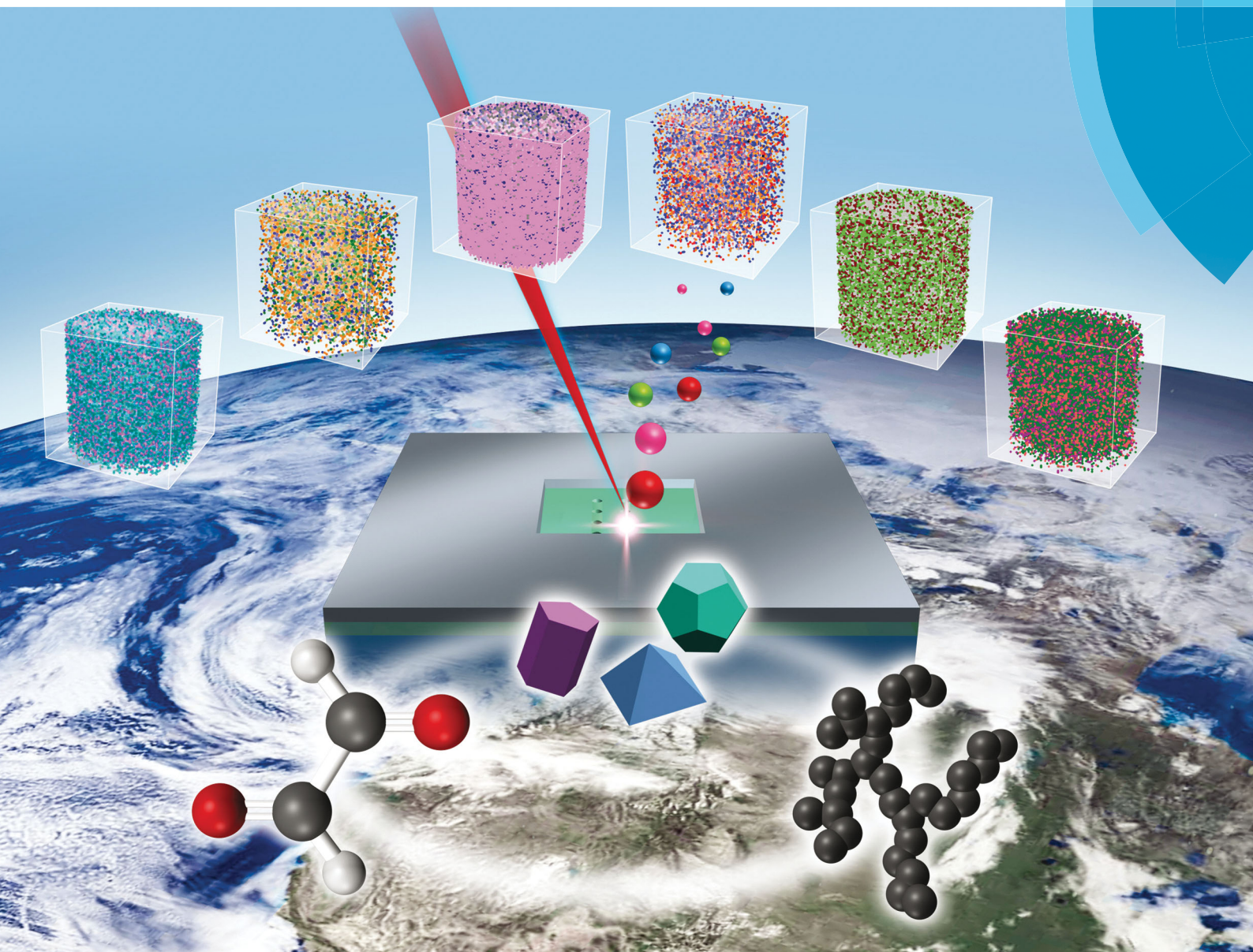


PCCP

Physical Chemistry Chemical Physics

rsc.li/pccp



ISSN 1463-9076



ROYAL SOCIETY
OF CHEMISTRY

PAPER

Jianmin Chen, Zihua Zhu, Xiao-Ying Yu *et al.*

Deciphering the aqueous chemistry of glyoxal oxidation with hydrogen peroxide using molecular imaging



Cite this: *Phys. Chem. Chem. Phys.*,
2017, **19**, 20357

Deciphering the aqueous chemistry of glyoxal oxidation with hydrogen peroxide using molecular imaging†

Xiao Sui, ^{ab} Yufan Zhou, ^{‡c} Fei Zhang, ^{‡bd} Jianmin Chen, ^{*ad} Zihua Zhu ^{*c}
and Xiao-Ying Yu ^{*b}

Aqueous surfaces after photochemical and dark reactions of glyoxal and hydrogen peroxide (H₂O₂) have been studied using a microfluidic reactor coupled with an *in situ* liquid time-of-flight secondary ion mass spectrometry (ToF-SIMS) for the first time. Spectral principal component analysis was used to determine similarities and differences among various photochemical aging and dark reaction samples and controls. Compared with previous results using bulk solutions, our unique liquid surface molecular imaging approach provided observations of glyoxal hydration (*i.e.*, first and secondary products), oxidation products (*i.e.*, glyoxylic acid, oxalic acid, formic acid, tartaric acid), oligomers, cluster ions, and water clusters with sub-micrometer spatial resolution. Observations of oxidation products give the physical foundation to deduce new reaction pathways at the aqueous surface. The first chemical mapping of water cluster changes between dark and photochemical aging suggests that glyoxal oxidation affects the hydrophobicity and water microenvironment at the surface, influencing the particle's ability of reactive uptake and subsequent cloud condensation nucleation and/or ice nucleation activation. Moreover, SIMS three-dimensional chemical mapping has made it possible to visualize the surface mixing state for the first time. We potentially provide a new method to investigate complex surface chemistry as an important source of aqueous secondary organic aerosol (aqSOA) formation in atmospheric chemistry.

Received 31st March 2017,
Accepted 23rd May 2017

DOI: 10.1039/c7cp02071f

rsc.li/pccp

Introduction

Organic aerosol (OA) particles affect climate change and human health. A large fraction of the OA burden is constituted by secondary organic aerosols (SOAs), which are believed to form by multi-phase oxidation.¹ It is known that heterogeneous chemistry in cloud water and aqueous aerosols are important sources of SOAs, collectively known as aqueous SOA (aqSOA).^{2,3} Water-soluble organic compounds can be highly oxidized by hydroxyl (OH) radicals to form products with low volatility in the aqueous phase that are largely retained in the solid phase,

likely contributing to the highest observed oxidation states of atmospheric OA.^{2,4} However, great uncertainty still remains in the pathways of how aqSOAs contribute to total OAs and their influence on aerosol properties such as their abilities to act as cloud condensation nuclei (CCN) and ice nuclei (IN) and subsequently affect the global climate radiative budget.⁵

Glyoxal, one of the simplest volatile organic compounds (VOCs), is a ubiquitous water-soluble gas-phase oxidation product in the atmosphere. It is considered as an important precursor for SOA formation.^{6,7} For example, glyoxal emission is 45 Tg year⁻¹ and its contribution to SOA formation is 2.6 Tg C year⁻¹.⁸ Observations compared with model studies in urban areas suggest that glyoxal can contribute to at least 15% of SOA formation.⁹ During cloudy days, approximately half of the atmospheric glyoxal is partitioned to the aqueous phase; subsequent uptake of glyoxal can be followed by hydration or formation of stable oxidation products.^{10,11} Glyoxal molecules mainly react with OH radicals and other oxidants. Hydrogen peroxide (H₂O₂) is the main source of OH radicals under UV conditions for studying glyoxal oxidation pathways.^{11–13}

Recent laboratory experiments and field observations suggest that more complex chemical reactions occur on the aqueous

^a Environment Research Institute, Shandong University, Jinan, 250100, China.
E-mail: jmchen@fudan.edu.cn

^b Earth and Biological Sciences Directorate, Pacific Northwest National Laboratory, Richland, WA 99354, USA. E-mail: xiaoying.yu@pnnl.gov

^c Environmental and Molecular Science Laboratory, Pacific Northwest National Laboratory, Richland, WA 99354, USA. E-mail: zihua.zhu@pnnl.gov

^d Shanghai Key Laboratory of Atmospheric Particle Pollution and Prevention, Fudan Tyndall Centre, Department of Environmental Science & Engineering, Fudan University, Shanghai 200433, China

† Electronic supplementary information (ESI) available. See DOI: 10.1039/c7cp02071f

‡ Equal contribution.

aerosol surface under both dark and photochemical conditions and contribute to SOA formation. For example, glyoxal aqueous oxidation reactions detected by high-performance liquid chromatography (HPLC) and electrospray ionization-mass spectrometry (ESI-MS) indicate that larger multifunctional products contribute to SOA formation.^{14,15} In addition, UV-visible orate and GC-MS were used to examine the existence of oligomers.^{16,17} The pathways of glyoxal oxidation in the aqueous phase under photochemical conditions are supported by model and laboratory experiments. First, glyoxal molecules go through hydration, and then they are oxidized to produce formic acid, glyoxylic acid and oxalic acid. Oxidation products will oligomerize to form dimers, trimers, and oligomers afterwards.^{12,18–20} The contribution to SOA formation *via* the dark reaction pathway should not be ignored either, because glyoxal can also be taken up into aerosols resulting in the formation of oligomers under dark conditions.⁷ Cloud relevant glyoxal concentration was about 10^{-4} M. It is known that high glyoxal concentration can lead to oligomer formation.^{11,12,18} A higher H_2O_2 concentration was used to approximate the pseudo-first order kinetic conditions for glyoxal as suggested in previous studies.^{12,21}

The aqueous surface chemistry differs from that in the bulk.^{22,23} For example, surface reactive uptake of glyoxal leads to significantly higher SOA mass;^{3,4} thus products from interfacial reactions at the aqueous surface are highly important to investigate the surface chemistry driven by photochemical and dark aging. However, direct probing of aqueous surface changes is a challenging task using surface sensitive techniques, because most surface analytical techniques are vacuum-based, not suitable to study liquids with high volatility.²⁴ Therefore, the ability to directly chemically map liquid surface changes as a result of photo or dark oxidation is needed to advance our understanding in atmospheric chemistry.

We have developed a unique vacuum compatible microfluidic reactor, the System for Analysis at the Liquid Vacuum Interface (SALVI), and enabled chemical imaging of liquid–vacuum and liquid–solid interfaces using time-of-flight secondary ion mass spectrometry (ToF-SIMS).^{25,26} An aperture of 2 μm diameter allows direct detection of the liquid surface. Surface tension holds the liquid within the aperture. SIMS as a powerful imaging technique can provide two-dimensional (2D) and three-dimensional (3D) images of the liquid surface and interface in addition to mass spectra with submicron spatial resolution.²⁷ We have employed this novel approach to study glyoxal oxidation by hydrogen peroxide at the aqueous surface under photochemical and dark aging for the first time in this work. Although ToF-SIMS has been widely used in the surface analysis of solid samples in materials science and biology,^{28,29} its applications in atmospheric chemistry have been limited.³⁰ This is the first systematic experimental effort focusing on atmospheric chemistry using *in situ* liquid SIMS.

We hypothesize that the H_2O_2 oxidation of glyoxal is dominant in the particle surface liquid layer (see Fig. S1, ESI† for an illustration) during reactive uptake, and that both dark and photochemical pathways contribute to SOA formation. Using the liquid–vacuum interface as an approximation of the liquid–air interface, the reaction pathways of H_2O_2 uptake by glyoxal

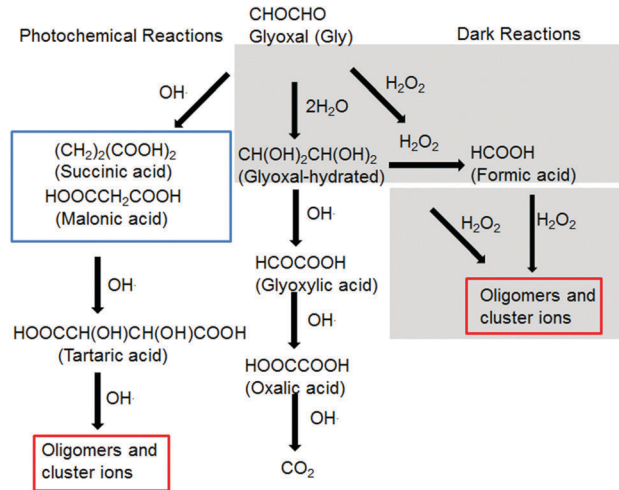


Fig. 1 The revised reaction flow chart of glyoxal and hydrogen peroxide oxidation at the aqueous surface adapted from Carlton *et al.*, 2007.¹² Gray shaded area indicates dark reactions. The red boxes highlight new reaction products found in this work. See Table S1 (ESI†) for product identification.

have been investigated at the liquid surface using *in situ* liquid SIMS for the first time. This work aims to improve the understanding of SOA formation contributions from dark and photochemical pathways, respectively (Fig. 1). SALVI is used as a batch reactor coupled with ToF-SIMS to image liquid surfaces. Molecular reactants and products at the liquid surface are directly observed at the molecular level. Moreover, many oxidation products from photochemical aging and dark reactions are found including water clusters, cluster ions, and oligomers, leading to the discovery of new reaction pathways. Water clusters at the liquid surface indicative of surface hydrophobicity and hydrophilicity as a result of dark and photochemical conditions have been observed for the first time. Because of the nature of SIMS spatial chemical mapping, 3D chemical images indicative of the surface mixing state have become possible using our unique molecular imaging approach.

Materials and methods

Sample preparation

A summary of the samples studied in this work is listed in the ESI,† Table S2. Fig. S2 (ESI†) shows the photochemical aging setup. A Hg–Ar UV lamp (ORIEL instruments, lamp model 6035, power supply model 6060) was used as the UV source; the wavelength was 253.65 nm. The distance between the silicon nitride (SiN) membrane and the lamp was set at 10 cm. When preparing for a photochemical reaction, glyoxal and hydrogen peroxide solutions were well mixed before being injected into the microchannel and were kept under the UV lamp immediately. The photochemical aging time reflected how long the sample was exposed under the UV lamp. Half an hour dark reaction time in the load lock chamber was indispensable for each of the photochemical aging samples. This was required to pump down to desirable vacuum. When preparing for a dark reaction sample, the solution mixed time was considered to include two sections (outside the SIMS instrument and in the load lock chamber).

SALVI and liquid SIMS

The microreactor fabrication details are reported in our previous publications.^{25,26} Briefly, soft lithography was used to make a $200\ \mu\text{m} \times 300\ \mu\text{m}$ (width \times depth) channel in a polydimethylsiloxane (PDMS) block. A $100\ \text{nm}$ thick SiN membrane ($1.5 \times 1.5\ \text{mm}^2$) supported on a silicon frame ($7.5 \times 7.5\ \text{mm}^2$) was irreversibly bonded with the PDMS block to form the detection area. Fig. 2A depicts the schematic setup of SALVI coupled with liquid SIMS; Fig. 2B–E represent multimodal SIMS data.

ToF-SIMS

A TOF-SIMS V spectrometer (IONTOF GmbH, Münster, Germany) was used. The pressure in the main vacuum chamber was maintained below 4×10^{-7} bar during the analysis.^{25,26} Before each analysis, the SiN window was cleaned by a $500\ \text{eV}\ \text{O}_2^+$ beam to remove impurities with a scanning area of $400 \times 400\ \mu\text{m}^2$. An electron flood gun was used to compensate surface charging. During experiments, a pulsed $25\ \text{keV}\ \text{Bi}_3^+$ primary ion beam was used with a current of $\sim 0.36\ \text{pA}$. The focus spot was about $0.45\ \mu\text{m}$ in diameter and the scan area was $\sim 2\ \mu\text{m}$. A pulse width of $150\ \text{ns}$ was used to punch through the SiN membrane. In the positive mode, it took about $350\ \text{s}$, and in the negative mode, about $400\ \text{s}$ to punch through the SiN membrane, respectively (Fig. 3 and Fig. S3, ESI[†]).³¹ The pulse width was changed to $50\ \text{ns}$ to obtain a relatively higher mass resolution in the latter portion of the depth profile. More experimental details are reported in our previous paper.³²

In this experiment, liquid did not keep flowing. Our recent papers^{32–35} have shown that the incident primary ion beam can provide enough energy to compensate energy loss caused by evaporation at the sputter interface, and reasonably strong and relatively stable molecular signals can be obtained. This indicates that flowing may not be necessary in liquid SIMS analysis. Because the sputter interface is dynamic, diffusion always exists. In 3D images reconstructed from depth profiling, the z -axis

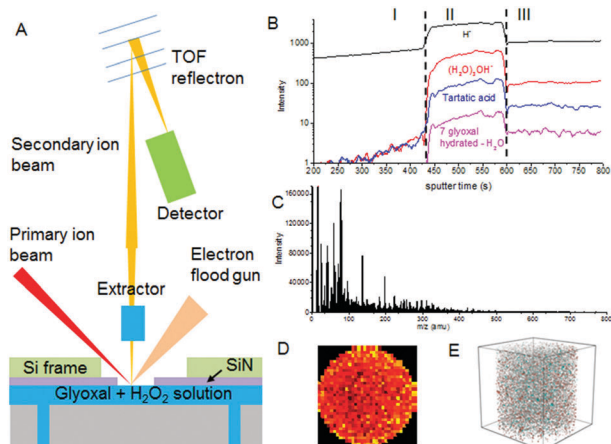


Fig. 2 (A) Liquid SIMS schematic setup enabled by SALVI. Four modes of measurements are possible including (B) depth profiling (C) m/z spectrum, (D) 2D image, and (E) 3D image. Gray represents $m/z\ 71\ (\text{H}_2\text{O})_3\text{OH}^-$, green $m/z\ 125\ (\text{H}_2\text{O})_6\text{OH}^-$, red $m/z\ 179\ (\text{H}_2\text{O})_9\text{OH}^-$.

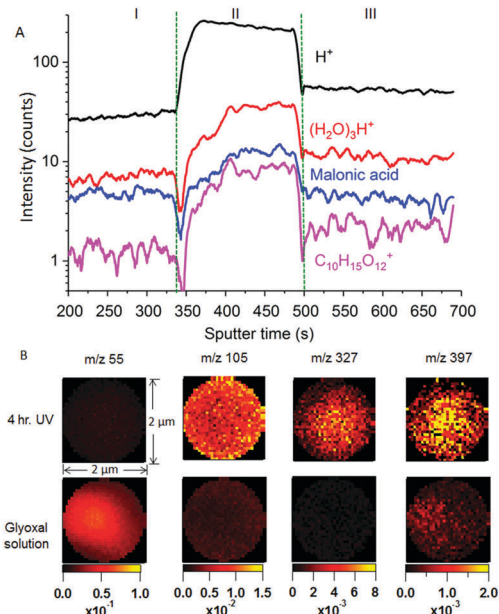


Fig. 3 (A) ToF-SIMS dynamic depth profiles of the 4 h UV aging sample. Region I refers to before SiN punch-through, region II wider pulse higher current for image reconstruction, and region III narrower pulse lower current for spectrum reconstruction. (B) 2D images in the positive mode. The ion intensity was normalized to total ions in B.

reflects the process from just drilling through the SiN membrane to reaching the asymptotic value, and the z -axis does not directly represent the depth as in solid samples. Instead they reflect the difference in chemical spatial distributions among samples at the surface layer.

Data were analyzed using the IONTOF software (SurfaceLab, version 6.3). Unit mass was used in data reduction. Mass calibration was done using CH_3^+ , C_2H_3^+ , C_3H_5^+ , C_4H_7^+ , and C_6H_5^+ in the positive spectra, and CH^- , CN^- , C_4H^- , and $\text{C}_6\text{H}_{13}\text{O}^-$ in the negative spectra, respectively.³⁶ Spectral principal component analysis (PCA) was conducted. Selected peaks used in the PCA are summarized in Table S3a and b (ESI[†]). In the selected peak spectral PCA, raw data were normalized to the total selected peak counts, square root transformed, and mean centered prior to spectral PCA analysis.³⁷ MATLAB R2014a (MathWorks, Natick, MA, USA) was used for PCA.

Results and discussions

Comparison between dry and liquid SIMS analysis

High mass resolution analysis using dry samples (*i.e.*, 4 h UV photochemical aging) was done to assist peak identifications in liquid-SIMS spectra. The details of dry sample preparation can be seen in the ESI[†] Fig. S4 (ESI[†]) shows the spectra of reference samples establishing the key peaks of products observed in this work using SIMS. Table S4 (ESI[†]) gives a summary of peak identification of these reference samples. Dry and wet samples were also compared. The mass to charge ratios (m/z) in dry and liquid SIMS were in good agreement, suggesting that the unit mass identification in liquid SIMS was reasonable.³⁸

Dynamic depth profiling

An example of SIMS dynamic depth profiling of a 4 h UV aging sample consisting initially of glyoxal and H₂O₂ in DI water is depicted in Fig. 3. Region I corresponds to the SiN membrane before punch through. In Fig. 3A, peaks characteristic of water (*i.e.*, (H₂O)₃H⁺, m/z^+ 55) showed a sharp increase at around 350 s, indicative of the SiN punch-through and observation of water in the positive mode.^{27,37,39} In region II, the intensity of representative ions of oxidation products, such as malonic acid (m/z^+ 105) and oligomers (*i.e.*, C₁₀H₁₅O₁₂⁺, m/z^+ 327), had higher intensity than region I, indicating observations of the reaction products at the surface. Region II lasted for about 150 s to collect data for image reconstructions. Then a narrower pulse (with reduced current, too) was used for collecting spectra with a relatively higher mass resolution in region III, in which signal intensity also went down.

Region II in the depth profile time series (Fig. 3A) was constructed for the comparison of 2D and 3D images to study the distribution of different products in glyoxal and H₂O₂ aqueous surface reactions. Four peaks relevant to glyoxal oxidation products were chosen to show representative 2D images in the positive mode (Fig. 3B), including a small water cluster ((H₂O)₃H⁺, m/z^+ 55), malonic acid (m/z^+ 105), a larger water cluster ((H₂O)₂₂H⁺, m/z^+ 397) and a 5 glyoxal dihydrate

oligomer (m/z^+ 327). The 2D images of water clusters showed different characteristics among photochemical reaction, dark reaction, and control samples. The photochemical reaction sample had lower counts of small water clusters than the dark reaction and control samples in the positive mode. However, higher counts of large water clusters in photochemical reaction samples than the other two scenarios were observed. In the negative mode, both small and large water cluster counts were higher in photochemical samples (Fig. S3b, ESI[†]). In the photochemical reaction sample, malonic acid (m/z^+ 105) had higher counts than those in dark reactions, indicating that it was one of the main products herein. The intensity of oligomer fragment peaks was higher in the UV treated sample, suggesting that oligomers were more likely to form under photochemical aging conditions compared to oxidation occurring under dark conditions.

Product identifications

ToF-SIMS positive ion mass spectra are depicted in Fig. 4 and additional spectra are shown in Fig. S5–S7 (ESI[†]). Identification of the key reactant and product peaks is listed in Table 1 and Tables S3, S5, S6 (ESI[†]). A glyoxal molecular peak (m/z^+ 59) was observed. This was challenging using ESI-MS. Orbitrap and FTICR mass analysers are the main stream mass analysers used for ESI-MS analysis; however, they are not sensitive to the

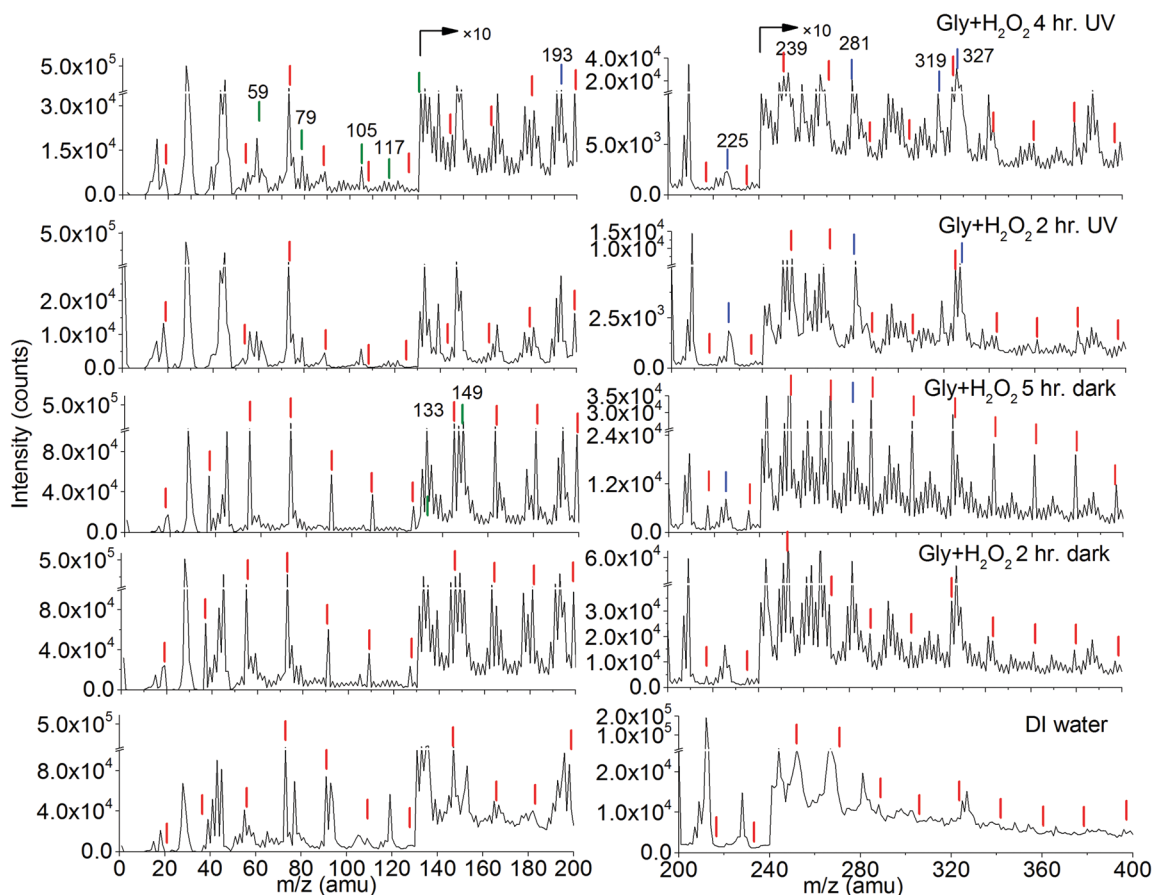


Fig. 4 ToF-SIMS spectral comparison of UV aging, dark reactions, and control samples in the positive ion mode (m/z 1–400). Red bars indicate the location of water cluster peaks, green oxidation products, and blue polymer fragments.

Table 1 (a) Peak identification of key reactants and products in the positive mode. (b) Peak identification of key reactants and products in the negative mode

m/z	Formula	Species	Ref.
(a)			
105	$C_3H_5O_4^+$	[Malonic acid + H] ⁺	18
119	$C_4H_7O_4^+$	[Succinic acid + H] ⁺	40
119	$C_3H_3O_5^+$	[Mesoxalic acid + H] ⁺	40
194	$C_6H_{10}O_7^+$	[Oligomer + H] ⁺	17
327	$C_{10}H_{15}O_{12}^+$	[Oligomer + H] ⁺	17
461	$C_{14}H_{21}O_{17}^+$	[Oligomer + H] ⁺	This study
521	$C_{18}H_{17}O_{18}^+$	[Oligomer + H] ⁺	This study
(b)			
45	CHO_2^-	[Formic acid - H] ⁻	12 and 19
73	$C_2HO_3^-$	[Glyoxylic acid - H] ⁻	12 and 19
79	$CH_3O_4^-$	[H ₂ O ···HCO ₃] ⁻	18
89	$C_2HO_4^-$	[Oxalic acid - H] ⁻	12
91	$C_2H_3O_4^-$	[Monohydrated glyoxylic acid - H] ⁻	12
133	$C_4H_5O_5^-$	[Malic acid - H] ⁻	1 and 14
149	$C_4H_5O_6^-$	[Tartaric acid - H] ⁻	14
163	$C_2H_3O_7^-$	[Hydroxymethanetricarboxylic-acid - H] ⁻	This study
249	$C_8H_9O_9^-$	[Oligomer - H] ⁻	17
265	$C_8H_9O_{10}^-$	[Cluster ion - H] ⁻	This study
422	$C_{14}H_{14}O_{15}^-$	[Oligomer - H] ⁻	17
437	$C_{12}H_{21}O_{17}^-$	[Oligomer - H] ⁻	This study
617	$C_{20}H_{25}O_{22}^-$	[Oligomer - H] ⁻	This study
635	$C_{19}H_{23}O_{24}^-$	[Oligomer - H] ⁻	This study
656	$C_{22}H_{24}O_{23}^-$	[Oligomer - H] ⁻	This study

detection of low mass ions, as discussed in previous studies.^{12,17} Products from glyoxal hydration and glyoxal and hydrogen peroxide oxidation, such as malonic acid (m/z^+ 105), and succinic acid/mesoxalic acid (m/z^+ 119) were observed in dark and photochemical aged samples. The peak intensities of these species were different between dark and photochemical reactions, suggesting that reactions with or without UV irradiation favours distinct pathways (Fig. 1). In contrast, these characteristic product peaks had low intensity in the control samples, indicating that these products were indeed formed as a result of dark or photochemical processing.

Oligomers and oxidation product cluster ions were also observed in both dark and photochemical aging samples (*i.e.*, m/z^+ 194, m/z^+ 461, m/z^+ 521). The formation of cluster ions, (*i.e.*, m/z^+ 193, m/z^+ 317) further illustrated the validity of using *in situ* liquid SIMS to study liquid surface reactions. Another exciting observation was strong water cluster peaks ($(H_2O)_nH^+$, $n \leq 44$) in the positive mode. In particular, the glyoxal and H₂O₂ 5 h dark reaction sample had strong water cluster peaks compared to DI water alone. The 4 h UV illuminated sample also showed higher water cluster intensities, significantly different from pure water.

Moreover, glyoxal hydration products were seen in the negative spectra, including m/z^- 75, glycolic acid/monohydrated glyoxal, m/z^- 91, monohydrated glyoxylic acid, and m/z^- 77, the glycolaldehyde dimer. Similar to the positive spectra, oligomers (m/z^- 223, m/z^- 311, m/z^- 422, m/z^- 572, m/z^- 617, m/z^- 635, m/z^- 656) were observed in the negative spectra. In addition, strong water cluster peaks $(H_2O)_nOH^-$ ($n \leq 43$) were seen. Similarly, the 5 h dark reaction sample showed strong water cluster peaks among others (see Fig. S7, ESI[†]). The summary of peak identifications is listed in Tables S3, S5 and S6 (ESI[†]).

Spectral PCA

Spectral PCA was conducted to elucidate the key components among SIMS m/z spectra in the positive and negative modes, respectively. Oxidation products, hydration products, cluster ions, oligomers, and water clusters peaks were selected in this analysis. The positive spectral PCA score and loading plots are depicted in Fig. 5. Additional score plots and loading plots are seen in Fig. S9–S12 (ESI[†]). Spectral PCA of all peaks was done to understand the data initially (see Fig. S13 and S14, ESI[†]).

Principal components (PC1 and PC2) explained 77% of all data in the positive ion mode. The PC1 vs. PC2 score plot showed distinctive clustering of the samples. The dark reaction samples contributed significantly to the positive PC1 loading, sharing common components in the negative PC2 loading. Short time UV reaction (*i.e.*, 15 min UV) products were similar to dark reactions. UV irradiated samples were largely separated from the dark reaction samples by PC1. Most of them were characterized by the negative PC1 loadings. Looking into the PC1 loading plot, water clusters, various oxidation products and oligomers were the main contributors. For example, oxidized products, such as hydrated glycolaldehyde (m/z^+ 79), malonic acid (m/z^+ 105), and glyoxal hydration related species (m/z^+ 149, $C_5H_9O_5^+$), were important peaks in the PC1 negative loading. The peaks contributing to positive PC1 were mainly small water clusters, $(H_2O)_nH^+$, $n = 2, 3, 5-9$. In contrast, larger water clusters had higher loadings in the negative PC1, thus they were more characteristic of UV irradiated samples. Similarly, larger water clusters ($(H_2O)_nH^+$, $n > 9$) contributed significantly to the negative PC2 loadings, indicating that the water microenvironment had been modified

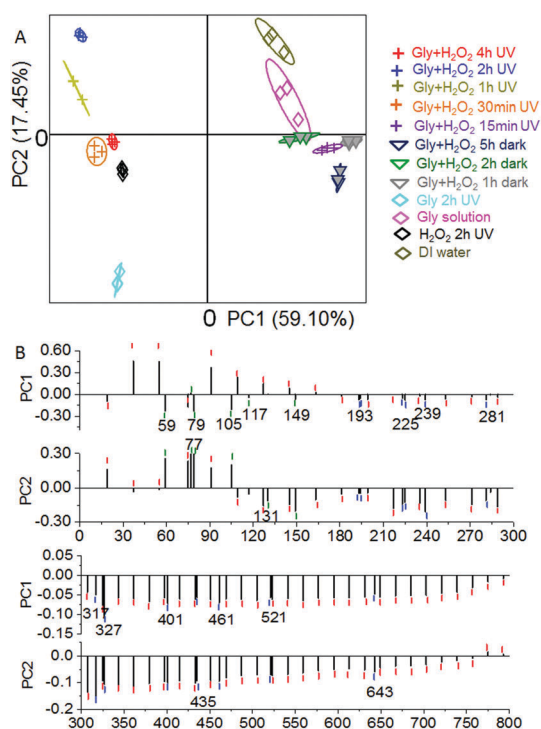


Fig. 5 Spectral PCA analysis in the positive ion mode. (A) PC1 vs. PC2 score plot and (B) PC1 and PC2 loading plots.

as a result of surface oxidation. In other words, glyoxal oxidation changed the surface water clusters as the aging time lengthened and conditions varied. Dark reactions favoured the formation of small water clusters and large water clusters tended to form under UV aging conditions.

Oxidation products (e.g., glyoxylic acid $m/z^+ 75$ (CHOCOOH)H⁺, glycolic acid $m/z^+ 77$ (CH₂OHCOOH)H⁺, malonic acid $m/z^+ 105$ C₃H₃O₄⁺), hydration products (glyoxal hydration species $m/z^+ 149$ C₄H₅O₆⁺), and oligomers (e.g., $m/z^+ 281$ C₈H₉O₁₁⁺, $m/z^+ 285$ C₈H₁₃O₁₁⁺, $m/z^+ 327$ C₁₀H₁₅O₁₂⁺, $m/z^+ 401$ C₁₂H₁₇O₁₅⁺, $m/z^+ 461$ C₁₄H₂₁O₁₇⁺, $m/z^+ 521$ C₁₈H₁₇O₁₈⁺) were the main peaks in PC1 negative loadings, indicating their importance in UV irradiated samples. Of specific interest was the finding of malonic acid as an important contributor to the negative PC1 loading, suggesting its role in photochemical aging.

The dark samples share commonalities in the negative PC2 loading. Glyoxal related species¹² ($m/z^+ 131$ C₅H₉O₅⁺) contribute to the negative PC2 loading, indicating their formation in dark and photochemical reactions. On the other hand, $m/z^+ 105$ malonic acid (a main contributor to the positive PC2) was more likely to form in the 1 h and 2 h UV treated samples. This result showed that photochemical aging time played a role in the formation of oxidation products. Oligomers, such as $m/z^+ 281$ C₈H₉O₁₁⁺, $m/z^+ 327$ C₁₀H₁₅O₁₂⁺, 5 glyoxal dihydrate, $m/z^+ 461$ C₁₄H₂₁O₁₇⁺, 7 glyoxal dihydrate · H₂O and $m/z^+ 643$, C₁₉H₃₁O₂₄⁺, were also important contributors to the PC2 negative loading. This finding suggested that oligomers were formed in both dark reactions and photochemical aging.

The negative ion mass spectral PCA score and loading plots are shown in Fig. S9 (ESI[†]). PC1, PC2, and PC3 explained over 88% of all data. Additional score plots and loading plots are provided in the ESI[†] (Fig. S12). Short-time dark reactions (i.e., 1 h, 2 h) share common features in the negative PC2 and PC3 loadings. They also showed similarities in samples which had undergone short-time UV photochemical irradiation (i.e., 15 min, 30 min, 1 h). In contrast, long-time UV and dark reactions were separated by PC3 positive. Peaks that had high loadings according to the negative PC2 include water clusters, the glycolaldehyde dimer $m/z^- 77$ (CH(OH)₂CH(OH)⁻), oxidation products (i.e., formic acid $m/z^- 45$ HCOO⁻), and oligomers (e.g., $m/z^- 151$ C₄H₇O₆⁻, $m/z^- 183$ C₄H₇O₈⁻, $m/z^- 185$ C₄H₉O₈⁻, $m/z^- 223$ C₆H₇O₉⁻, $m/z^- 437$ C₁₂H₂₁O₁₇⁻, $m/z^- 483$ C₁₃H₂₃O₁₉⁻, $m/z^- 572$ C₁₈H₂₀O₂₁⁻, $m/z^- 617$ C₂₀H₂₅O₂₂⁻, 10 gly dihydrate, $m/z^- 635$ C₂₂H₁₉O₂₂⁻, 10 gly dihydrate-2H-2H₂O, $m/z^- 656$ C₂₂H₂₄O₂₃⁻, 11 gly dihydrate). Water cluster peaks, with the exception of $n = 9, 13, 17, 18, 33, 36$, had high negative PC2 loadings, indicating that the water microenvironment of surfaces after dark reactions and short UV photochemical aging had changed compared to bulk water. Peaks that were the main contributors to the positive PC2 included various glyoxal oxidation products (i.e., acetic acid $m/z^- 59$ CH₃COO⁻, malonic acid $m/z^- 103$ C₄H₅O₅⁻).

PC3 distinguished long-time (> 2 h) dark reactions and photochemical aging samples from short-time (≤ 2 h) dark reactions and UV aging. Shorter dark reaction times and photochemical reaction times shared common oxidation products, for example, formic acid ($m/z^- 45$), glycolic acid ($m/z^- 75$) and

oxidation products (i.e., $m/z^- 79$ CH₃O₄⁻) were key contributors to the negative PC3 loading. The peaks with high negative PC3 loadings were complementary to the findings deduced from the PC2 analysis. In addition, peaks that had high loadings in PC3 positive provided further insight of the product differences as a result of aging time. Oxidized oligomers (e.g., $m/z^- 249$, $m/z^- 311$, $m/z^- 363$, $m/z^- 422$, $m/z^- 572$, $m/z^- 617$) and various cluster ions (e.g., $m/z^- 265$, $m/z^- 329$) all contributed positively to PC3. This implied that long-time reactions under both dark and photochemical conditions favoured the formation of oligomers, known to be essential to SOA formation.

Overall, negative and positive spectral PCA results were in agreement. Namely, dark reactions and photochemical aging seemed to lead to different products and water clusters from the glyoxal and H₂O₂ aqueous surface oxidation. These results suggested that photochemical aging and dark reactions had distinct reaction pathways. The revised reaction flow chart and pathways are summarized in Fig. 1. Moreover, our results showed that reaction time was an important factor in the intermolecular interactions reflected in the water microenvironment (i.e., size and distribution of water clusters) differences and oxidation products. The latter included a variety of redox products, oligomers, hydrates and cluster ions.

In order to study the difference of glyoxal oxidation products, bar plots of key oxidization products, oligomers and water clusters both in positive and negative modes are shown in Fig. S15 and S16 (ESI[†]). Data were normalized to the selected total ions in both the positive and negative modes. More glyoxal related species ($m/z^+ 131$)¹² and hydrated glyoxal related species ($m/z^+ 149$) were observed in the 5 h dark sample, while malonic acid ($m/z^+ 105$) had high intensity among UV samples compared to the water control and samples undergoing dark aging (Fig. S15, ESI[†]). See Table S3a and b (ESI[†]) for peak identification. Short-time dark reactions had lower counts in oxidation product peaks, the control sample had even lower counts in products, implying that UV processing and aging time could influence the degree of glyoxal oxidation. In comparison with photochemical reactions, more H₂O · HCO₃ ($m/z^- 79$, CH₃O₄⁻) anions were observed in the 4 h UV and 5 h dark sample, suggesting that glyoxal could be oxidized to CO₂ given the longer reaction time. In Fig. S11 and S12 (ESI[†]), more oligomers were observed in the UV exposed sample. Complimentary to this finding, glyoxal dihydrate oligomers in the negative mode were more likely to form under long-time UV photochemical conditions and dark reactions.

Water clusters were another interesting and important observation (see additional PCA results in Fig. S11 and S12, ESI[†]). Photochemical aging seems to induce different water affinities, which includes larger water clusters, while small water clusters are more likely encountered in dark reactions than in UV associated reactions.

Reaction pathways

Based on the 2D image comparison, spectral PCA, and bar plot analysis, revised pathways of aqueous surface glyoxal oxidations are suggested as illustrated in Fig. 1. It was known that dark and photochemical reactions can contribute to the formation

of SOA.^{4,12,19} Our results were in agreement with these earlier findings, namely, various oxidation products were found in the glyoxal aqueous surface reaction with hydrogen peroxide under different conditions. Carboxylic acid products (*i.e.*, formic acid, glyoxylic acid, oxalic acid, malonic acid, tartaric acid), hydration products (*i.e.*, glyoxal hydration, glyoxylic acid hydration) were observed (Fig. 4). Succinic acid (m/z^+ 119), and malonic acid (m/z^+ 105) have been first observed in the UV sample. A possible acid-catalyzed dehydration reaction for the formation of malonic acid was proposed in a previous work,¹⁸ this was confirmed by our observation. However, the peaks associated with this finding in the photochemical aging process were not observed in dark reactions.

Succinic acid, mesoxalic acid, malic acid, and malonic acid were also reported as a result of glyoxal oxidation with the OH radical *via* ESI-MS and HPLC-UV.^{14,40} Another previous experiment suggested that malonic acid could be an important intermediate in the oligomer formation.²⁰ However, due to its high volatility, formic acid was not expected to contribute to the formation of SOA. Using our *in situ* molecular imaging tool, formic acid (m/z^- 45) has been proposed to participate in the formation of complex oligomers, for instance $C_8H_{13}O_{11}^-$, m/z^- 285 and $C_9H_{11}O_{12}^-$, m/z^- 311 in dark reactions.

Under dark conditions, a previous model study suggested the formation of oligomers and high molecular weight products might lead to an overestimate of SOA formation.⁷ A chamber study using an aerosol mass spectrometer detected the formation of glyoxal oligomers of up to m/z 175.⁶ Our results showed that glyoxal oxidation products were likely to form more complex dehydrate oligomers with higher m/z peaks. Therefore, cluster ions indicative of ion pairs formed *via* weak intermolecular forces were likely to be significant players in photochemical reactions in the aqueous phase. Various glyoxal hydration products and oligomers were quite important under dark conditions.

In situ measurements provide more reliable results compared to dry sample analysis.³⁸ Compared to HPLC-UV, no organic solvents are needed to extract chemical compounds. No other sample preparation steps are required. Compared with ESI-MS, ours can provide molecular imaging including glyoxal, hydration products, oxidation products, oligomers, cluster ions, and water clusters at the liquid surface. The observation of cluster ions, water clusters, carboxylic acids, and oligomers is useful to decode the complex reaction mechanism at the liquid surface. Our results demonstrate that the reactive H_2O_2 uptake by glyoxal at the aqueous surface can be investigated by SALVI enabled liquid ToF-SIMS. Such capability is useful for investigating complex liquid surface reactions of importance in atmospheric chemistry.

Surface water cluster and cluster ions formation

Although hydrophobic forces, hydrogen bonds, and van der Waals forces are weak intermolecular interactions, they are quite important in many interfacial processes in atmospheric chemistry, such as reactions at the air–water interface and oxidation of surface organics.^{41,42} Our results provide direct evidence of these important intermolecular interactions at the aqueous surface by observing hydration products and cluster

ions with water molecules in both the positive and negative ion modes, some of which have been only possible using our approach for the first time. Water clusters have been used as models for the theoretical study of reactions at the aqueous surface,⁴³ our study has confirmed the formation of water clusters and their variations in UV aging and dark reactions. Our results show that water forms large clusters in the UV aging process while small water clusters are mainly observed in dark reactions. Moreover, water could participate in the oxidation reaction and formation of hydrated products at the aqueous surface. The observation of cluster ions (*e.g.*, m/z^+ 149, m/z^+ 239, m/z^+ 317, m/z^- 183, m/z^- 241, m/z^- 325, m/z^- 329) indicated that weak intermolecular interactions could play a significant role in modifying the surface structure and reactivity.

The van der Waals interaction is a weak force between two dipoles or one permanent dipole and one transient dipole nearby molecules. Water molecules can form clusters with many atmospheric species by van der Waals interactions and hydrogen bonding.⁴³ Water clusters can be observed in pure water as shown in Fig. 4 and Fig. S6 (ESI[†]). However, water clusters are much more predominant in the glyoxal and hydrogen peroxide solutions either after UV aging or dark reactions. This indicates that they not only form *via* the hydrogen bonding between the oxygen atoms of products and adjacent water molecules but also *via* hydrogen bonding of the surrounding water molecules. Once water clusters form, they tend to increase in size; however at high temperature, water clusters are predicted to break down in order to increase the entropy of the system.⁴⁴ In this study, the temperature effect was insignificant, since the experiments were done at room temperature. Therefore, the occurrence of large water clusters should be related to the oxidation products after photochemical or dark aging.

Atmospheric species including inorganic and organic acids, aldehydes, and ketone are known to form molecular complexes with water molecules due to van der Waals interactions, dipolar interactions and hydrogen bonding to decrease the energy of a system.⁴³ Although higher hydrophobicity exists at the surface after UV aging, oxidation products can form hydrated products in a small molecule regime (about 20 carbon atoms in the molecules).⁴⁵ Such products were also observed in dark reactions including glyoxal dehydrate products (*i.e.*, m/z^+ 327, m/z^+ 461, m/z^- 183, m/z^- 241) and cluster ions with water molecules (*i.e.*, m/z^+ 319, m/z^+ 435, m/z^- 241, m/z^- 285) in both positive and negative modes, implying that water was able to form a stabilized state with glyoxal oxidation products.

Water affinity is roughly defined as the frequency of hydrates that form chemical functional groups with water.²² Many product peaks related to hydrates were observed in this work, for example, monohydrated glyoxylic acid (m/z^- 91). Oligomer products also show water affinity, such as m/z^+ 327, m/z^+ 461, and m/z^+ 521. Moreover, previous studies indicated that oligomers could form due to glyoxal hydration.¹⁷ Our SIMS spectral results showed strong evidence of products related to water affinity, such as water addition of m/z^- 223 to form the peak at m/z^- 241, and also the water addition of m/z^- 437 to form the species at m/z^- 455.

As seen in the spectral PCA results, both small and large water clusters show different occurrences in dark and photochemical reaction samples. This result suggests that the oxidation products favour the formation of small water clusters after surface aging, especially under dark reaction conditions. The tendency of water cluster formation also depends on the hydrophilic and hydrophobic properties of the solid surface. When the water cluster size increases, the hydrophobicity of the surface increases accordingly.^{41,46,47} Our results show that larger water clusters are prevalent after surface aging both in the positive and negative modes, implying that the oligomer formed at the surface tends to induce higher hydrophobicity. Our PCA results indicate that large water clusters tend to form under UV photochemical aging leading to more hydrophobic surfaces. In contrast, small water clusters are more likely to be produced under dark reactions leading to more hydrophilic surfaces. This finding implies that different reaction conditions have a significant impact on the surface reactivity. For example, a particle undergoing UV aging *vs.* dark aging would have almost opposite water affinity, affecting its ability to uptake or repel water molecules. Such phenomena have direct applications in the particle's ability to act as CCN or IN in the atmosphere.

3D imaging and surface mixing state

The mixing state is defined as the distribution of the chemical species spatial compositions in each particle.⁴⁸ It is an important parameter in atmospheric aerosol simulations and observations.^{49,50} However, the detailed mixing state at the particle surface is often

not available or incomplete by direct physical measurements for ambient aerosols.⁵⁰ The glyoxal air–liquid surface reactions contribute a lot to the aqSOA formation,¹⁹ yet the surface mixing states remain unknown. Our results have provided the first surface mixing state visualization by using *in situ* imaging mass spectrometry.

Reconstructed 3D images of various products, including carboxylic acids, oligomers, water clusters, and cluster ions are illustrated in Fig. 6. Replicate 3D images are depicted in Fig. S17 (ESI[†]). The images are normalized to the total ion counts. The intensity of each colour is proportional to the relative ion percentage, that is, darker colour indicates higher spatial counts. The spatial distribution and molecular ion intensities are different between the UV aging and dark reaction samples. In the positive mode, more small water clusters were observed at the dark aged surface (*i.e.*, $(\text{H}_2\text{O})_3\text{H}^+$). These smaller water clusters tend to distribute on the external part of the liquid surface.

For example, $(\text{H}_2\text{O})_6\text{H}^+$ is more external than $(\text{H}_2\text{O})_{11}\text{H}^+$. However, in the photochemical aged sample, the water cluster distribution is opposite. For example, $(\text{H}_2\text{O})_{11}\text{H}^+$ is more external than $(\text{H}_2\text{O})_6\text{H}^+$ and $(\text{H}_2\text{O})_3\text{H}^+$ (Fig. 6A). Large water clusters were also observed in photochemical aging samples. For instance, $(\text{H}_2\text{O})_{31}\text{H}^+$ and $(\text{H}_2\text{O})_{35}\text{H}^+$ distributed more externally on the UV aged surface (Fig. 6B). The water cluster distribution showed that larger water clusters tended to form under UV conditions, which indicated higher hydrophobicity existed on the surface. The 3D water cluster spatial distribution is consistent in the negative ion mode (Fig. 6G–M).

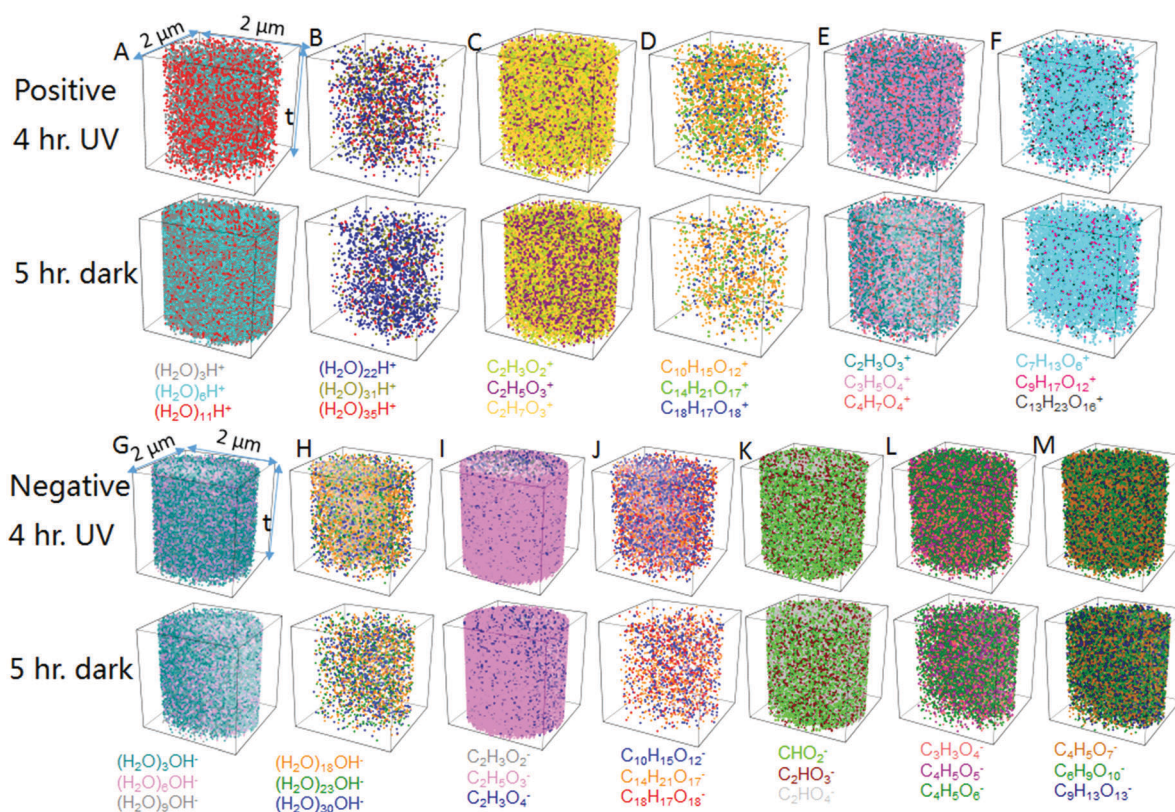


Fig. 6 3D images of photochemical aging and dark reaction reactants and products in the positive (A–F) and negative (G–M) ion modes showing the surface mixing state.

Oxidation products also show different spatial chemical distributions. For example, glyoxylic acid mainly appears at the liquid surface under photochemical reaction conditions, but it is more internal in dark reactions. Formic acid, oxalic acid, and malonic acid are well-mixed under UV conditions (Fig. 6E, K and L). However, oxalic acid tends to distribute more externally in dark processing (Fig. 6K). Tartaric acid is more intense in the photochemical aging process (Fig. 6L) and thus it is more likely to participate in surface aqSOA formation with UV irradiation. Glycolaldehyde dimers (Fig. 6I) and glycolaldehyde hydrated (Fig. 6C) are both evenly distributed on the UV and dark aged surfaces. In comparison, succinic acid and malonic acid distribute externally in photochemical and dark aged samples (Fig. 6E). Through dark or photochemical processing, oligomers tend to be well mixed (Fig. 6D and J). More oligomers are observed under UV conditions in both negative (Fig. 6J) and positive (Fig. 6F) modes, suggesting that photochemical aging is favourable for SOA formation. This finding is consistent with the PCA results.

Other examples are the hydration products and cluster ions. In the positive mode, glyoxal and glycolic acid (Fig. 6C) are well mixed. Cluster ions, indicative of the formation of ion pairs that are important products related to van der Waals interactions at the aqueous surface, seem to be better mixed in dark aging (Fig. 6M). UV aging reactions favour the formation of cluster ions with H₂O molecules (*i.e.*, C₆H₉O₁₀⁻ and C₉H₁₃O₁₃⁻) compared to the dark reaction.

Water clusters show a significant distinction under different conditions (Fig. S19a and b, ESI[†]). UV photolysis and dark aging have stronger water cluster intensity than the controls (*i.e.*, DI water, glyoxal solution with 2 h UV illumination, and glyoxal solution). Small water clusters (*i.e.*, m/z^+ 55 (H₂O)₃H⁺, m/z^+ 109 (H₂O)₆H⁺, m/z^+ 199 (H₂O)₁₁H⁺; m/z^- 71 (H₂O)₃OH⁻, m/z^- 125 (H₂O)₆OH⁻, m/z^- 179 (H₂O)₉OH⁻) tend to form in dark aging. Large water clusters (*i.e.*, m/z^+ 397 (H₂O)₂₂H⁺, m/z^+ 559 (H₂O)₃₁H⁺, m/z^+ 631 (H₂O)₃₅H⁺, m/z^- 341 (H₂O)₁₈OH⁻, m/z^- 431 (H₂O)₂₃OH⁻, m/z^- 557 (H₂O)₃₀OH⁻) are more likely to form by UV photolysis. Our results indicate that UV photolysis promotes the hydrophobicity of the microenvironment at the aqueous surface.

Overall, 3D images demonstrated that reaction conditions play an important role in the mixing state of the water microenvironment and chemical spatial distribution. UV aging tends to form more SOA products than dark aging. Both modify the surface mixing states. Such spatial chemical visualization is useful to better understand how glyoxal oxidation contributes to SOA formation and facilitate simulation and process model development.

Conclusions

We have employed a novel molecular imaging tool, namely *in situ* liquid SIMS enabled by a microfluidic reactor, to study glyoxal surface oxidation chemistry. Our results show that H₂O₂ oxidation of glyoxal provides an important avenue for aqueous SOA formation under photochemical aging and dark reactions.

Many oxidation products (*i.e.*, carboxylic acids), hydration products, cluster ions, and oligomers have been observed by *in situ* surface imaging mass spectrometry. New reaction products have been identified based on liquid SIMS spectra, suggesting expanded reaction pathways.

The observation of oligomers suggested that both UV aging and dark reaction can be significant contributors to aqSOA formation. Another significant finding was the relationship between water clusters and the hydrophobic/hydrophilic properties of the surfaces treated with and without UV illumination. They were significantly different between photochemical aging and dark reactions, or compared with bulk water. The PCA results showed that more large water clusters existed in UV aging, suggesting that such surface aging tends to be more hydrophobic. In contrast, the surface which had undergone dark reactions could be more hydrophilic. Such findings could provide useful information to unlock the puzzle of aerosol reactive uptake and its implications for CCN and IN activation due to surface reactions.

The observation of cluster ions suggested that the water microenvironment could affect oxidation pathways and ultimately aqSOA formation. More importantly, the particle surface mixing state could be visualized by 3D mapping. Spatial chemical distribution of key reactants and products at the surface can provide first-hand physical measures for process model development and improve the mechanistic understanding of aqueous surface reactions. Our results demonstrated that the unique portable microfluidic reactor combined with liquid SIMS could be a powerful tool to investigate aqueous surface reactions *in situ* at the molecular level and fill in the knowledge gap of interfacial reactions involving liquids in atmospheric chemistry.

Acknowledgements

Support for this work was from the Pacific Northwest National Laboratory (PNNL) Materials Synthesis and Simulation across Scales (MS3) Initiative-Laboratory Directed Research and Development (LDRD) and the Earth and Biological Sciences Directorate (EBS) Mission Seed LDRD fund. The research was performed in the W. R. Wiley Environmental Molecular Sciences Laboratory (EMSL), a national scientific user facility sponsored by the Office of Biological and Environmental Research (BER) and located at PNNL.

References

- 1 B. Ervens, B. J. Turpin and R. J. Weber, *Atmos. Chem. Phys.*, 2011, **11**, 11069–11102.
- 2 J. L. Woo, D. D. Kim, A. N. Schwier, R. Li and V. F. McNeill, *Faraday Discuss.*, 2013, **165**, 357.
- 3 C. Knote, A. Hodzic and J. L. Jimenez, *et al.*, *Atmos. Chem. Phys.*, 2014, **14**, 6213–6239.
- 4 V. F. McNeill, *Environ. Sci. Technol.*, 2015, **49**, 1237–1244.
- 5 C. R. Hoyle, G. Myhre, T. K. Berntsen and I. S. A. Isaksen, *Atmos. Chem. Phys.*, 2009, **9**, 2715–2728.
- 6 M. M. Galloway, P. S. Chhabra, A. W. H. Chan, J. D. Surratt, R. C. Flagan, J. H. Seinfeld and F. N. Keutsch, *Atmos. Chem. Phys.*, 2009, **9**, 3331–3345.

- 7 M. M. Galloway, C. L. Loza, P. S. Chhabra, A. W. H. Chan, L. D. Yee, J. H. Seinfeld and F. N. Keutsch, *Geophys. Res. Lett.*, 2011, **38**, L17811.
- 8 T.-M. Fu, D. J. Jacob, F. Wittrock, J. P. Burrows, M. Vrekoussis and D. K. Henze, *J. Geophys. Res.*, 2008, **113**, D15303.
- 9 R. Volkamer, F. San Martini, L. T. Molina, D. Salcedo, J. L. Jimenez and M. J. Molina, *Geophys. Res. Lett.*, 2007, **34**, L19807.
- 10 F. Schweitzer, L. Magi, P. Mirabel and C. George, *J. Phys. Chem. A*, 1998, **102**, 593–600.
- 11 Y. B. Lim, Y. Tan and B. J. Turpin, *Atmos. Chem. Phys.*, 2013, **13**, 8651–8667.
- 12 A. G. Carlton, B. J. Turpin, K. E. Altieri, S. Seitzinger, A. Reff, H.-J. Lim and B. Ervens, *Atmos. Environ.*, 2007, **41**, 7588–7602.
- 13 L. Schone and H. Herrmann, *Atmos. Chem. Phys.*, 2014, **14**, 4503–4514.
- 14 A. L. Corrigan, S. W. Hanley and D. O. Haan, *Environ. Sci. Technol.*, 2008, **42**, 4428–4433.
- 15 D. O. De Haan, A. L. Corrigan, M. A. Tolbert, J. L. Jimenez, S. E. Wood and J. J. Turley, *Environ. Sci. Technol.*, 2009, **43**, 8184–8190.
- 16 A. N. Schwier, N. Sareen, D. Mitroo, E. L. Shapiro and V. F. McNeill, *Environ. Sci. Technol.*, 2010, **44**, 6174–6182.
- 17 W. P. Hastings, C. A. Koehler, E. L. Bailey and D. O. De Haan, *Environ. Sci. Technol.*, 2005, **39**, 8728–8735.
- 18 Y. B. Lim, Y. Tan, M. J. Perri, S. P. Seitzinger and B. J. Turpin, *Atmos. Chem. Phys.*, 2010, **10**, 10521–10539.
- 19 B. Ervens and R. Volkamer, *Atmos. Chem. Phys.*, 2010, **10**, 8219–8244.
- 20 M. J. Perri, S. Seitzinger and B. J. Turpin, *Atmos. Environ.*, 2009, **43**, 1487–1497.
- 21 A. K. Y. Lee, P. Herckes, W. R. Leitch, A. M. Macdonald and J. P. D. Abbatt, *Geophys. Res. Lett.*, 2011, **38**, L11805.
- 22 P. Jungwirth, B. J. Finlayson-Pitts and D. J. Tobias, *Chem. Rev.*, 2006, **106**, 1137–1139.
- 23 P. Jungwirth and D. J. Tobias, *J. Phys. Chem. B*, 2002, **106**, 6361–6373.
- 24 X. Y. Yu, B. W. Liu and L. Yang, *Microfluid. Nanofluid.*, 2013, **15**, 725–744.
- 25 L. Yang, X. Y. Yu, Z. H. Zhu, T. Thevuthasan and J. P. Cowin, *J. Vac. Sci. Technol., A*, 2011, **29**, 061101.
- 26 L. Yang, X. Y. Yu, Z. H. Zhu, M. J. Iedema and J. P. Cowin, *Lab Chip*, 2011, **11**, 2481–2484.
- 27 X. Hua, C. Szymanski and Z. Wang, *et al.*, *Integr. Biol.*, 2016, **8**, 635–644.
- 28 J. S. Fletcher and J. C. Vickerman, *Anal. Chem.*, 2013, **85**, 610–639.
- 29 S. Fearn, *Mater. Sci., Tech. Ser.*, 2015, **31**, 148–161.
- 30 A. Laskin, D. J. Gaspar, W. H. Wang, S. W. Hunt, J. P. Cowin, S. D. Colson and B. J. Finlayson-Pitts, *Science*, 2003, **301**, 340–344.
- 31 J. C. Yu, Y. F. Zhou, X. Hua, Z. H. Zhu and X.-Y. Yu, *J. Visualized Exp.*, 2016, e53708, DOI: 10.3791/53708.
- 32 Y. Zhou, J. Yao and Y. Ding, *et al.*, *J. Am. Soc. Mass Spectrom.*, 2016, 1–8, DOI: 10.1007/s13361-016-1478-x.
- 33 J. C. Yu, Y. F. Zhou, X. Hua, S. Q. Liu, Z. H. Zhu and X.-Y. Yu, *Chem. Commun.*, 2016, **52**, 10952–10955.
- 34 Z. Wang, Y. Zhang, B. Liu, K. Wu, S. Thevuthasan, D. R. Baer, Z. Zhu, X.-Y. Yu and F. Wang, *Anal. Chem.*, 2017, **89**, 960–965.
- 35 Y. Ding, Y. Zhou, J. Yao, C. Szymanski, J. Fredrickson, L. Shi, B. Cao, Z. Zhu and X.-Y. Yu, *Anal. Chem.*, 2016, **88**, 11244–11252.
- 36 F. M. Green, I. S. Gilmore and M. P. Seah, *J. Am. Soc. Mass Spectrom.*, 2006, **17**, 514–523.
- 37 X. Hua, M. J. Marshall, Y. J. Xiong, X. Ma, Y. F. Zhou, A. E. Tucker, Z. H. Zhu, S. Q. Liu and X.-Y. Yu, *Biomicrofluidics*, 2015, **9**, 031101.
- 38 X. Sui, Y. Zhou, F. Zhang, Y. Zhang, J. Chen, Z. Zhu and X.-Y. Yu, *Surf. Interface Anal.*, 2017, submitted.
- 39 X. Hua, X. Y. Yu and Z. Y. Wang, *et al.*, *Analyst*, 2014, **139**, 1609–1613.
- 40 Y. Tan, M. J. Perri, S. P. Seitzinger and B. J. Turpin, *Environ. Sci. Technol.*, 2009, **43**, 8105–8112.
- 41 P. Jungwirth and D. J. Tobias, *Chem. Rev.*, 2006, **106**, 1259–1281.
- 42 B. J. Finlayson-Pitts, *Phys. Chem. Chem. Phys.*, 2009, **11**, 7760–7779.
- 43 V. Vaida, *J. Chem. Phys.*, 2011, **135**, 020901.
- 44 Z. S. Nickolov, N. Goutev and H. Matsuura, *J. Phys. Chem. A*, 2001, **105**, 10884–10889.
- 45 D. Chandler, *Nature*, 2005, **437**, 640–647.
- 46 E. V. Krisilova, T. V. Eliseeva and G. Y. Oros, *Colloid J.*, 2011, **73**, 72–75.
- 47 T. Ohba, H. Kanoh and K. Kaneko, *J. Am. Chem. Soc.*, 2004, **126**, 1560–1562.
- 48 N. Riemer and M. West, *Atmos. Chem. Phys.*, 2013, **13**, 11423–11439.
- 49 H. Fu, M. Zhang, W. Li, J. Chen, L. Wang, X. Quan and W. Wang, *Atmos. Chem. Phys.*, 2012, **12**, 693–707.
- 50 V. Aquila, J. Hendricks and A. Lauer, *et al.*, *Geosci. Model Dev.*, 2011, **4**, 325–355.